Photovoltaic thermal system design including aquifer thermal energy storage in a fifth generation district heating network in Hilversum

Beijneveld, Ties; Alpízar-Castillo, Joel; Ramírez-Elizondo, Laura

DOI
10.1016/j.csite.2025.105854

Publication date
2025

Document Version
Final published version

Published in
Case Studies in Thermal Engineering

Citation (APA)
Beijneveld, T., Alpízar-Castillo, J., & Ramírez-Elizondo, L. (2025). Photovoltaic thermal system design including aquifer thermal energy storage in a fifth generation district heating network in Hilversum. *Case Studies in Thermal Engineering*, *68*, Article 105854. https://doi.org/10.1016/j.csite.2025.105854

Case Studies in Thermal Engineering 68 (2025) 105854

Contents lists available at ScienceDirect

Case Studies in Thermal Engineering

journal homepage: www.elsevier.com/locate/csite

Photovoltaic thermal system design including aquifer thermal energy storage in a fifth generation district heating network in Hilversum

Ties Beijneveld, Joel Alpízar-Castillo *, Laura Ramírez-Elizondo

DC Systems, Energy Conversion and Storage Group, Delft University of Technology, Mekelweg 6, Delft, 28 CD, Zuid Holland, The Netherlands

HIGHLIGHTS

- A PVT+ATES system is investigated to minimize grid usage in a Dutch 5GDHN case study.
- A single ATES well, rather than distributed systems, is optimal.
- Large ATES maintain a stable, colder temperature, maximizing COP in heat pumps.
- Optimal configurations reduce power purchase and support the energy infrastructure.

GRAPHICAL ABSTRACT

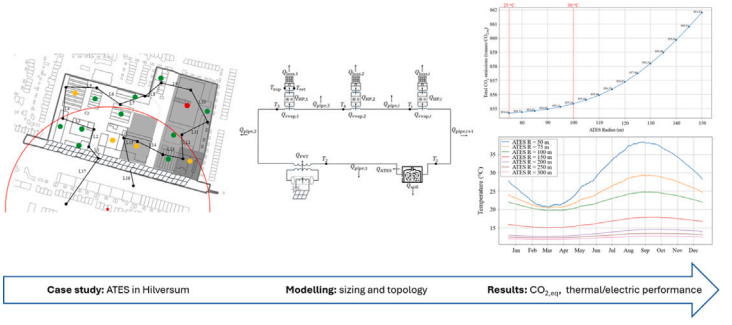

ARTICLE INFO

Keywords:
Aquifer thermal energy storage
Multi-carrier energy system
Fifth-generation district heating network
Photovoltaic thermal system

ABSTRACT

The urgent need to address global warming and transition to sustainable energy solutions has driven the development of innovative heating systems. Among those solutions, several district heating alternatives have been proposed to combine heat pumps and thermal energy storage tanks. This paper addresses the integration of photovoltaic thermal systems (PVT) with aquifer thermal energy storage (ATES) within a fifth-generation district heating network as an innovative combination to minimise electrical power consumption from the grid, thereby reducing grid dependency and CO_2 emissions. The proposed configuration is tested for the Werfgebied district in Hilversum, the Netherlands A Python model of the multi-energy carrier system is developed to investigate the effects of configuration, storage distribution, and component sizing within the district heating network, embedding the thermal and electrical behaviour of the components and their interaction. The results show that an optimal configuration for the ATES and PVT combination involves a single ATES well rather than distributed thermal energy storage. The results indicate that the aquifer's size significantly affects the overall operating temperature

* Corresponding author.
E-mail address: j.j.alpizarcastillo@tudelft.nl (J. Alpízar-Castillo).

https://doi.org/10.1016/j.csite.2025.105854
Received 13 November 2024; Received in revised form 1 February 2025; Accepted 6 February 2025
Available online 17 February 2025

and its fluctuations. A larger ATES maintains a stable but relatively colder temperature. If constrained by a maximum allowed ATES temperature of 20 ° C, the optimal ATES size is 175 000 m^3; however, when considering the overall benefit and excluding that constraint, the optimal system size comprises an ATES of 380 000 m^3 and an 800 module PVT system, reducing the overall emissions by 856 tonnes of CO_2 equivalent compared to the case without the district heating.

1. Introduction

The escalating challenges of global warming and the urgent need for sustainable energy solutions have led to the development of a fifth-generation district heating network (5GDHN) in Hilversum, Netherlands. This pioneering initiative is a collaboration between the company HET and the municipality of Hilversum. It features the integration of a photovoltaic-thermal (PVT) carport, positioning it at the forefront of innovative energy systems. This project leverages renewable energy sources to provide sustainable district heating.

The urgency of transitioning away from fossil fuels and reducing greenhouse gas emissions has never been more clear. With the world's primary energy consumption heavily dependent on non-renewable sources, the resultant environmental impact underscores the necessity for a shift towards more sustainable and resilient energy systems. Globally, fossil fuels constitute 80% of the total energy supply [1]. In the Netherlands, this figure rises to 84% for total energy consumption. Within the domestic sector in the Netherlands, 15% of energy originates from solar or wind sources [2]. The necessary energy transition aligns with the global commitments outlined in the United Nations' Sustainable Development Goals and the Paris Agreement, which aim to limit global warming to well below 2 degrees Celsius above pre-industrial levels.

The European Union and the Netherlands have embarked on ambitious paths to reduce their carbon footprints and transition towards renewable energy sources. In this context, the implementation of district heating networks, especially 5GDHNs, offers a promising avenue for enhancing energy efficiency, reducing carbon emissions, and easing overall network congestion. By integrating low-temperature operations with renewable energy technologies such as photovoltaic thermal modules, thermal storage, and heat pumps, 5GDHNs represent a significant advancement in district heating systems. This integration optimises energy distribution and lessens the strain on electrical grids, contributing to a more resilient and efficient energy infrastructure.

1.1. Case study

This research focuses on the current building landscape and forthcoming construction plans in the Werfgebied, Hilversum-Oost (The Netherlands). There, the collective Vereniging Duurzaam Werfgebied is currently identifying opportunities for sustainable development and energy efficiency improvements, aiming to make the district energy-neutral by 2028 [3]. The project studied in this work is a fifth-generation district heating network for residential buildings equipped with water-to-water heat pumps, including the sizing and technical analysis of an aquifer thermal energy storage system coupled to a photo-voltaic thermal system located on the roof of a carport.

To create a representative approximation of the district in Hilversum, the sizes of the buildings and pipes need to be implemented. The buildings were grouped into three categories: small, medium, and large (see Table 1), based on data provided in [3]. The annual energy consumption was estimated per building to create a different electric load profile. Then, the map of the Hilversum Werf is used to approximate the length of the tubes in the district heating network. The map shown in Fig. 1 shows the route of the pipes and the categories of buildings. The lengths of the pipes are summarised in Table 2. Note that this map shows only the carport connection, as it will be constructed at that location; the location and sizes for the ATEs will be discussed in Sections 3 and 4. The model parameters can be consulted in [4].

1.2. Relevant literature

The inclusion of fossil-fuel-free heating technologies has gained momentum in recent years. In particular, heat pumps (HP) have been the preferred alternative to gas boilers for residential and commercial buildings. However, the deployment of heat pumps has caused congestion in distribution networks, in addition to scheduling challenges given fluctuating energy prices and the high energy consumption of heat pumps [5]. For this reason, thermal energy storage (TES) has emerged as an equivalent to electrical storage to shift the peaks in energy consumption and ensure thermal comfort [6].

Several thermal energy storage technologies have been proposed in the literature, classified into three main types: sensible heat, latent heat, and chemical heat storage [7]. Sensible heat storage stores the thermal energy in a medium that changes its temperature without changing its phase. In contrast, latent heat storage takes advantage of the phase change in certain materials. Conversely, chemical heat storage uses reversible chemical reactions, similar to electric batteries. A detailed review of those technologies was done in [8], concluding that sensible heat alternatives present the lowest energy density, typically below 100 kWh/m^3. Latent heat storage, in the form of phase change materials, presents a wide temperature range, from 0 ° C to over 200 ° C, with energy densities

Nomenclature

(k)	Current timestep
$(k \pm i)$	ith timestep

Abbreviations

5GDHN	5-gen district heating network
ATES	Aquifer thermal energy storage
PVT	Photovoltaic thermal
TESS	Thermal energy storage System

Variables

α	Absorbance
$\dot{m}$	Mass flow
$\dot{Q}$	Thermal power
$\dot{V}$	Volumetric flow
ϵ	Emissivity
η	Efficiency
ρ	Density
τ	Transmittance
A	Area
c	Specific thermal capacity
d	Diameter
E	Electric energy
G	Solar irradiance
h	Total heat transfer coefficient
h^{cond}	Conductive heat transfer coefficient
h^{conv}	Convective heat transfer coefficient
h^{r}	Radiative heat transfer coefficient
k	Thermal conductivity
L	Length
m	Mass
N	Number of PVT tubes
n	Number of PVT modules
p	Pressure losses
Q	Thermal energy
q	Airflow
R	Thermal resistance
r	Radius
T	Temperature
t	Time
U	Internal energy
u	Wind speed
v	Velocity
COP	Coefficient of performance

ranging from 50 kWh/m^3 to 250 kWh/m^3. Chemical heat storage showed the highest energy densities, ranging from 150 kWh/m^3 to 600 kWh/m^3, with a similar temperature range than latent heat storage (from 40 ° C to 200 ° C). Nevertheless, there is also a trade-off between performance and cost. The total system costs for sensible heat storage ranging from 0.1 €/kWh and 10 €/kWh, whereas latent heat storage ranges between 10 €/kWh and 50 €/kWh, and chemical heat storage between 8 €/kWh and 100 €/kWh. In the context of district heating networks, as the one presented in this work, sensible heat storage in the form of an ATES seems very attractive, thanks to the lower costs and volume availability given the underground nature of the solution. However, in contexts with higher volumetric constraints, latent or chemical heat storage might be a more suitable solution, for instance, as part of the heating, ventilation, and air conditioning systems in buildings [9].

This work aims to design, size and optimise a district heating system in residential areas with a case study in Hilversum, specifically targeting CO_2 emissions reduction. This involves a comprehensive analysis of how various component sizes and storage

Fig. 1. Map of the heating network in Hilversum Werf, indicating the building categories.

Table 1
Parameters of the different building sizes [10].

Parameter	Building category			Units
	Small	Medium	Large	
Length	35	50	70	m
Width	25	30	40	m
Height	6	7	8	m
Roof area	874	1,504	3,130	m^2
Glass area	213	400	647	m^2
Annual energy consumption	54,455	72,283	285,836	kWh

Table 2
Pipe lengths.

Parameter	L1	L2	L3	L4	L5	L6	L7	L8	L9	L10	L11	L12	L13	L14	L15
Value (m)	30	30	45	45	50	50	30	30	50	60	50	40	30	50	30

distribution influence power consumption from the grid to the electrical components, affecting CO_2 emissions. With the application of 5GDHN, the methodology incorporates PVT systems and ATES. The integration of PVT and ATES within 5GDHN frameworks is relatively novel, presenting various unexplored aspects. A literature search was conducted to establish a solid foundation on the existing knowledge on this combination, focusing on studies that utilise both PVT and ATES. The specific query in the Scopus database was 'ATES OR "Aquifer Thermal Energy Storage" AND PVT OR "Photovoltaic Thermal".'

Khlebnikova et al. [11] explored using PVT combined with 5GDHN, water-to-water heat pumps, and ATES in Haarlem, Netherlands. This study focuses on the system's control strategy. It considers a decentralised PVT system and emphasises on the control system within the household, recommending network temperatures between 14 ° C (during winter) and 18 ° C (during summer). Jansen et al. [12] discussed designing a sustainable urban energy system in Haarlem to create an energy-neutral neighbourhood, considering multiple technologies and district heating networks, utilising decentralised PVT, HPs, and ATES. Their study considered different isolation levels for the buildings, and carbon intensities for the grid energy, and concluded that network temperatures between 20 ° C and 40 ° C minimise energy consumption, therefore, the CO_2 emissions. Picone et al. [13] evaluated the performance of various ATES pilot sites across Europe, including a project in Delft that integrates ATES with PVT systems. This study provides valuable performance data and operational insights from different European contexts, demonstrating the compatibility of ATES and PVT technologies, leading to savings in gas of up to 63 %.

The aforementioned studies utilise a combination of PVT and ATES but have a different scope than this work. On the one hand, both Khlebnikova [11] and Jansen [12] explore decentralised PVT installations on individual households, whereas this research focuses on a centralised PVT system installed on a carport. On the other hand, [13] proposes a brief review of some ATES pilot projects in Europe without providing much detail about the electric or thermal performance of the district heating network. Additionally, all these papers employ differing methodologies and pursue different objectives. In contrast, we aim to analyse the effects of the distribution of the ATES and the impact of different component sizes. We also included a sizing analysis to minimise

the CO_2 emissions from the district heating network. These aspects have not been addressed in the mentioned papers.

To design an optimal low-temperature district heating network utilising PVT and ATES, the initial step involves designing the topology of the network. This process includes evaluating two scenarios for locating the ATES, considering one with centralised ATES and another with distributed ATES. Significant research has explored the effects of distributed heat storage within district heating networks. Jebamalai [14] analyses the cost and efficiency implications of centralised versus distributed thermal storage within a thermal network, highlighting cost reductions associated with distributed storage configurations. Roder [15] developed an optimisation tool in Python using Mixed Integer Linear Programming (MILP) for low-temperature district heating networks, focusing on economic optimisation to reduce thermal losses and operational costs. Nuytten [16] examines a multi-carrier energy system, analysing the impact of centralised versus distributed thermal energy storage. The study notes that distributed storage reduces power supply flexibility for combined heat and power (CHP) systems, due to variability among storage tanks. While these studies are closely related in terms of thermal energy distribution, they focus on thermal energy storage systems (TESS) in general instead of specifically ATES, which is the focus of this work.

The second step in the system's design involves sizing the components. This includes determining the optimal dimensions for the ATES system(s) and the quantity of PVT modules to be installed. Initially, the performance of various component sizes will be analysed for both centralised and distributed storage systems, focusing on heat generation and loss. Third, the sizes of the PVT system and ATES will be adjusted to minimise CO_2 emissions. This strategy seeks to derive an optimal design that enhances the system's autonomy. Previous research has made significant contributions to sizing optimisation in district heating networks using PVT. Geraedts [17] discusses the combination of PVT with 5GDHN and TESS, employing MILP for cost and environmental optimisation, focusing on sizing TESS. Krishna Priya [18] explores the optimal sizing of a PVT system in conjunction with thermal storage and load, focussing on cost-effectiveness. Testi [19] examines a PVT system combined with thermal storage for a residential building, including economic considerations in the sizing process.

1.3. Contribution

This work contributes by designing and optimising a district heating system in residential areas with a case study in Hilversum, specifically targeting CO_2 emissions reduction. The contributions, identified after addressing the research gap in Section 1.2, using a case scenario of a 5GDHN in Hilversum, the Netherlands, are as follows:

- investigate the network's performance when a centralised or distributed ATES are coupled, from a thermal (ATES and distribution network thermal losses) and electrical (heat pumps and ATES pumping electric consumption) perspective, and
- analyse the sizing effects of a centralised PVT installation in combination with ATES in the ATES and distribution network thermal losses, the heat pumps electric consumption, grid exchange and equivalent CO_2 emissions.

In addition, all our models and simulations were done in Python, which are open-access and available for calculating district heating networks, including PVT, buildings, piping, ATES and heat pumps.

1.4. Methods

First, we require a framework to model the system's components: the PVT, the ATES, the HP, the distribution networks and the thermal demand. Section 2 provides the mathematical description used in this work based on the models available in the literature. Second, in Section 3, we analysed how different storage distributions and configurations of district heating and ATES affect thermal performance. Multiple cases were constructed for this purpose: one utilising a single, centralised ATES unit in various configurations and the other employing multiple, smaller, distributed ATES units. The distributed ATES units will be smaller in size but greater in number, totalling the same volume of water compared to the centralised ATES. The feasibility of installing these ATES units will be determined based on the capabilities of the existing area. This approach will enable a comprehensive assessment of thermal losses and the overall performance of the distribution scenario.

Third, the size of the PVT and ATES systems were studied in different scenarios for both distributed and centralised ATES configurations. We highlighted the influence of these changes on the system's generation capability and temperature stability over the year. This involves creating a feasible region of scenarios, each with specific dimensions, configurations, and ATES location, while considering the physical constraints of the project, as shown in Section 4. Finally, the optimal component sizes for the systems are proposed to ensure reliability and minimise CO_2 emissions. These emissions will be directly linked to the electrical use and generation of the components resulting from the system's thermal behaviour. This electrical power flow results in power extracted from the grid to operate the system. An objective function will be created to minimise CO_2 emissions, considering the number of PVT modules and the sizes of the ATES units. The constraints will be based on the available area and the findings from the component size analysis.

2. Mathematical framework

2.1. Photovoltaic-thermal system

The PVT system considered is a liquid-based PVT module. The module comprises multiple layers: a glass top, an air gap, the PV, thermal absorber and thermal fluid tubes [20]. Each layer exchanges heat due to conduction, convection or radiation. The method of expressing the thermodynamic behaviour is derived from [20,21], describing the heat transfer in each layer depending on the adjacent layers or atmosphere. To simplify, the following assumptions were made:

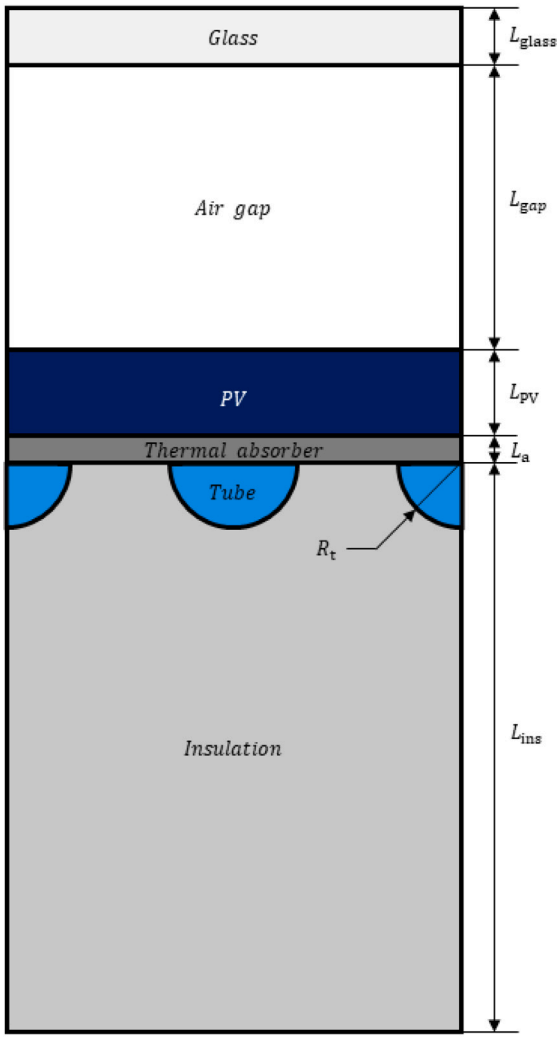

Fig. 2. Cross section of the PVT collector.

- the edges are well insulated, with no heat loss,
- the layers are very thin, so there is negligible vertical heat conduction,
- no dust or shading effects are considered, and
- the flow rate of the fluid is constant.

The analysed layers are the glass, PV, thermal absorber and fluid. It is assumed that the air layer and thermal absorber temperatures are not relevant [20]. Thermal energy is transferred between the layers and the atmosphere through conduction, convection, and radiation. Note that the PV layer consists of multiple layers: glass, two layers of EVA, the Si cell, the Tedlar layer, and an adhesive [21]. Fig. 2 shows a cross-section of the PVT collector layers. The different heat transfer processes in the PVT are divided into different layers. First, the glass layer receives solar irradiation, a part is reflected the rest is absorbed or transmitted to the PV layer. The glass layer receives reflected radiation and radiative losses from the PV layer. Thereby, it loses heat due to convection caused by wind. The PV layer receives solar radiation, of which some is reflected to the glass layer and some is absorbed. The radiation to the glass is heat loss from the PV layer. Convection between the PV and the glass layer also occurs due to the air gap. Some of the irradiation absorbed by the PV layer is converted into electricity. The heat absorber layer exchanges heat with the PV layer, the insulation and the fluid through convection. The insulation loses heat to the environment through convection from the wind. The heat transfer in the fluid in the tubes is also caused through convection by the pumping system [20].

The energy balance equations for the different layers are rearranged by isolating the temperatures of the glass layer, PV layer, thermal absorber layer and the fluid: T_{glass}, T_{PV}, T_a and T_{fluid}. This gives the following set of equations [21]

$$\begin{cases} T_{glass}(k+1) = C_1(k)T_{glass}(k) + C_2(k)T_{PV}(k) - D_1(k) \\ T_{PV}(k+1) = C_3(k)T_{glass}(k) + C_4(k)T_{PV}(k) + C_5(k)T_a(k) - D_2(k) \\ T_a(k+1) = C_6(k)T_{PV}(k) + C_7(k)T_a(k) + C_8(k)T_f(k) - D_3(k) \\ T_f(k+1) = C_9(k)T_a(k) + C_{10}(k)T_f(k) - D_4(k) \end{cases}, \tag{1}$$

The system of equations in (1) allows one to estimate the temperatures of each layer of the PVT as a function of the heat transfer coefficients. The temperature of the glass layer for the next time step $k+1$ depends on the current temperature of the glass and pv layers, the convective transfer coefficient with the surrounding air h^{conv}_{glass}, the radiative heat transfer coefficient from the sun h^{r}_{glass}, the convective heat transfer coefficient with the air gap between the glass layer and the PV layer h_{gap}, the radiative heat transfer coefficient caused from the glass to the PV layer $h^{r}_{glass\text{-}PV}(k)$, and the absorbance α_{glass} of the glass. The previous terms have been conveniently grouped per layer as

$$C_1(k) = \frac{A_{glass}\Delta t}{m_{glass}c_{glass}}\left[\frac{m_{glass}c_{glass}}{A_{glass}\Delta t} - h^{conv}_{glass}(k) - h^{r}_{glass}(k) - h_{gap}(k) - h^{r}_{glass\text{-}PV}(k)\right], \tag{2}$$

$$C_2(k) = \frac{A_{glass}\Delta t}{m_{glass}c_{glass}}\left[h_{gap}(k) + h^{r}_{glass\text{-}PV}(k)\right], \tag{3}$$

and

$$D_1(k) = \frac{A_{glass}\Delta t}{m_{glass}c_{glass}}\left[h^{conv}_{glass}T_{amb}(k) + h^{r}_{glass}(k)T_{sky}(k) + \alpha_{glass}G(k)\right]. \tag{4}$$

For the PV layer, the same analysis is done, where its future state depends on the current temperature of the glass, PV and thermal absorber layers, the convective heat transfer coefficient with the air gap between the glass layer and the PV layer h_{gap}, the radiative heat transfer coefficient caused from the glass to the PV layer $h^{r}_{glass\text{-}PV}(k)$, the conductive heat transfer coefficient between the PV and the thermal absorber layers h^{cond}_{PV-a}, the transmittance of the glass layer τ_{glass}, the absorbance of the PV layer α_{PV}, and the energy absorption efficiency of the PV cells η_{PV}, grouped as

$$C_3(k) = \frac{A_{PV}\Delta t}{m_{PV}c_{PV}}\left[h_{gap}(k) + h^{r}_{glass\text{-}PV}(k)\right], \tag{5}$$

$$C_4(k) = \frac{A_{PV}\Delta t}{m_{PV}c_{PV}}\left[\frac{m_{PV}c_{PV}}{A_{PV}\Delta t} - h_{gap}(k) - h^{r}_{glass\text{-}PV}(k) - h^{cond}_{PV-a}(k)\right], \tag{6}$$

$$C_5(k) = \frac{A_{PV}\Delta t}{m_{PV}c_{PV}}h^{cond}_{PV-a}(k), \tag{7}$$

and

$$D_2(k) = \frac{A_{PV}\Delta t}{m_{PV}c_{PV}}\alpha_{PV}\tau_{glass}G(k)\left[1 - \eta_{PV}(k)\right]. \tag{8}$$

For the thermal absorber layer, the future temperature depends on the current temperatures of the PV, the thermal absorber and the fluid layers, the conductive heat transfer coefficient between the PV and the thermal absorber layers h^{cond}_{PV-a}, the total heat transfer coefficient between the thermal absorber and the fluid h_{a-f}, and the heat transfer coefficient between the absorber and the ambient h^{cond}_{a}, grouped as

$$C_6(k) = \frac{A_a\Delta t}{m_a c_a}h^{cond}_{PV-a}(k), \tag{9}$$

$$C_7(k) = \frac{\Delta t}{m_a c_a}\left[\frac{m_a c_a}{\Delta t} - h^{cond}_{PV-a}(k)A_a - h_{a-f}(k)A^{abs}_t - h^{cond}_{a}(k)A_a\right], \tag{10}$$

$$C_8(k) = \frac{\Delta t}{m_a c_a}h_{a-f}(k)A^{abs}_t, \tag{11}$$

and

$$D_3(k) = \frac{A_a\Delta t}{m_a c_a}h^{cond}_{a}(k)T_{amb}(k). \tag{12}$$

Finally, the future temperature of the fluid depends on the previous temperature of the thermal absorber and fluid layers, and the total heat transfer coefficient between the thermal absorber and the fluid h_{a-f}, grouped as

$$C_9(k) = \frac{A^{abs}_t\Delta t}{m_f c_f}h_{a-f}(k), \tag{13}$$

$$C_{10}(k) = \frac{\Delta t}{m_f c_f}\left[\frac{m_f c_f}{\Delta t} - h_{a-f}(k)A^{surf}_t - 2\dot{m}_f c_f\right], \tag{14}$$

and

$$D_4(k) = 2\frac{\Delta t}{m_f}\dot{m}_f T_f^{in}(k). \tag{15}$$

The remaining constants are the area, mass, specific heat and thickness of the ith layer A_i [m^2], m_i [kg], c_i [J/kg], and L_i [m], respectively; the mass flow of the fluid in the tube per time step is $\dot{m}_f$ [kg/s]. In addition, A_t^{abs} [m^2] is the area of the tube which is in contact with the absorber, A_t^{surf} [m^2] is the tube's lower surface area which is in contact with the isolation layer. G [Wm^{-2}] is the solar irradiation and T_{amb} is the ambient temperature [21]. The difference in temperature over time is expressed discretely, $T_i(k+1)$ is the temperature $T_i(k)$ [° C] after time step Δt [s]. T_{sky} is the equivalent radiative temperature of the sky. There are multiple equations and methods to define the equivalent radiative temperature of the sky. In this case, the Brunt model is used [22].

The heat output of the PVT modules can be calculated using the temperature of the fluid in the tubes

$$\dot{Q}_{PVT}(k) = \eta_T N \dot{m}_f c_f \left[T_f^{out}(k) - T_f^{in}(k)\right] = 2\eta_T N \dot{m}_f c_f \left[T_f(k) - T_f^{in}(k)\right] \tag{16}$$

where η_T is the efficiency of the heat exchanger from the PVT to the heating network and N is the number of tubes in the PVT.

2.2. Aquifer thermal energy storage

The ATES comprises an underground water-bearing layer (aquifer) for thermal energy storage. This system adopts a doublet ATES configuration, wherein the cooling and heating wells are installed in separate boreholes. A specific horizontal distance is carefully maintained to prevent interference between the two. During winter, water is cooled by the thermal demand of the building and then directed into the cold well after its use. Conversely, in the summer, the water heated by the building's cooling requirements is stored in the warm water well, ready for use in the following winter. This cyclical process facilitates an efficient use of underground thermal energy, contributing to the sustainability and energy efficiency of residential heating and cooling systems.

Due to the aquifer's significantly smaller height than the area, the aquifer's heat losses are attributed exclusively to thermal diffusion towards the overburden and underburden layers [23]. The applicable temperature in the ground surrounding an ATES system is assumed to be constant and not dependent on the environment. At a certain depth, typically between 4 to 6 m, the ground temperature becomes relatively constant and remains unaffected by annual environmental changes [24], but solely depends on geothermal energy. This principle holds true in the Netherlands, where ATES systems are usually installed at depths ranging from 20 m to 150 m, a range considered relatively shallow yet sufficiently deep to negate environmental influences [25]. Measurements in Hilversum indicate a stable temperature of 11 °C at both 25 m and 125 m depths [26], suggesting no significant temperature variation occurs within this subsurface span.

In the context of the Hilversum ATES, the depth of the wells demonstrates a similarity. The aquifer under Hilversum is positioned between two impermeable layers, consisting of clay and fine sand, preventing water from permeating them. This aquifer stretches to depths varying from approximately 45 m to 65 m and extends to around 148 m to 170 m. Due to the presence of toxic pollution water at shallower depths, a minimum operational depth of 110 m is maintained for the aquifer's use [27]. Consequently, the operational depth range for the well in this aquifer lies between 110 m and 170 m. Based on this setup, it is assumed that the temperature within this specified depth range remains constant at 11 °C, aligning with the observed stable temperature characteristics at similar depths within the region.

The aquifer's heat balance comprises the heat supplied by the water inlet, the heat withdrawn by the water outlet, and heat losses to the surrounding overburden and underburden geological formations. The ATES is an open system, so the input and output heat are expressed as the flow of warm water given by

$$\dot{m}_{in} c_f T_{in}(k) - \dot{m}_{out} c_f T_{ATES}(k) - \dot{Q}_{soil}(k) = \sum_{i=1}^{n} m_i c_i \frac{\Delta T_{ATES}}{\Delta t}, \tag{17}$$

where $\dot{m}_{in}$ is the mass flow into the ATES, with temperature T^{in}. $\dot{m}_{in}$ is the mass flow from the ATES, with temperature T_{ATES}. $\dot{Q}_{soil}$ is the heat exchange with surrounding underground layers. m_i and c_i are the mass and specific heat of the aquifer material. The aquifer is assumed to consist of water and rock; thus, the internal heat depends on these materials' ratio, [23], given by

$$\sum_{i=1}^{n} m_i c_i = (1-n) m_r c_r + n m_f c_f, \tag{18}$$

where n is the porosity of the aquifer, m_r and m_f the mass of the rock and water, c_r and c_f the heat capacity of rock and water.

Under the assumption that the aquifer behaves like a perfectly mixed water tank, the temperature within the ATES can be modelled using

$$T_{ATES}(k+1) = T_{ATES}(k) + \frac{\Delta t[\dot{m}_{in} c_f T_{in}(k) - \dot{m}_{out} c_f T_{ATES}(k) - \dot{Q}_{soil}(k)]}{(1-n) m_r c_r + n m_f c_f}. \tag{19}$$

The total heat loss to the ground can be split into heat loss into the overburden and underburden layers.

$$\dot{Q}_{soil} = \dot{Q}_{overburden} + \dot{Q}_{underburden} \tag{20}$$

with

$$\dot{Q}_{overburden} = h_{ATE-o}^{cond} A_{top} \left[T_{ATE}(k) - T_{overburden}\right] \tag{21}$$

and

$$\dot{Q}_{\text{underburden}} = h^{\text{cond}}_{\text{ATE-u}} A_{\text{bottom}} \left[T_{\text{ATE}}(k) - T_{\text{underburden}}\right]. \tag{22}$$

where $h^{\text{cond}}_{\text{ATE-o}}$ and $h^{\text{cond}}_{\text{ATE-u}}$ can be calculated with the method proposed in [21]. The method proposes a discretisation of the soil around the thermal storage as a semi-infinite solid with one-dimensional coordinates, using as boundary conditions the surface temperature and the mean effective temperature at a point underground where the effects of surface heating are neglectable.

Water extraction and injection into aquifers require the installation of pumps for each ATES well. These pumps consume electricity, similar to the operation of heat pumps within the system. Considering a constant pump efficiency and constant volume flow of water, the power consumption of these hydraulic pumps can be calculated using

$$P_{\text{ATES}} = \frac{\dot{V}(\rho g h + L p_L)}{\eta_{\text{ATES}}}, \tag{23}$$

where $\dot{V}$ represents the volume flow rate of water, with ρ, g, and h, denoting the density of water, the gravitational constant, and the vertical distance traversed. L signifies the length of the underground pipe, while η_{ATEP} is the efficiency of the pump [28]. The unit p_L represents the pressure loss per unit length within the pipe; this can be calculated using

$$p_L = \frac{64}{Re}\left(\frac{L}{\text{d}}\right)\left(\frac{\rho_f v^2}{2}\right). \tag{24}$$

Here, Re is the Reynolds number of the fluids' flow and v is the velocity. The length of the tube is L and the diameter is d.

2.2.1. Heat pumps

Water-to-water heat pumps are used, where the heat pump extracts thermal energy from a water supply. To determine the amount of power necessary to meet heating demand, the coefficient of performance is calculated using the model proposed by [29] as

$$\text{COP}(k) = 7.90471 e^{-0.024(T_{\text{ret}}(k) - T_{\text{in}}(k))}. \tag{25}$$

The constants were established by regression of 10 different heat pump models. Here, T_{ret} is the return temperature of the fluid at the inlet of the heat pump, which is cooled by the thermal demand of the building and T_{in} is the inlet temperature of the district heating into the heat pump.

Typically, the practical COP is lower than the theoretical values reported in the datasheets, and expressions can lead to unrealistic COPs. For this reason, we considered that the heat pump uses R32 refrigerant [30], which has a typical maximum COP of 3.6 for water-to-water systems [31]; this way, we capped Eq. (25) to a maximum value of 3.6. The heat pumps' heat to evaporate the refrigerant is extracted from the water in the district heating network. This extracted heat can be calculated with [32]

$$\dot{Q}_{evap}(k) = \dot{Q}_{\text{HP}}(k)\left(1 - \frac{1}{\text{COP}(k)}\right). \tag{26}$$

Similarly, the heat supply of the heat pumps can be expressed using a similar method as the PVT

$$\dot{Q}_{\text{HP}}(k) = \eta_{\text{HP}} \dot{m}_f c_f \left(T_{\text{sup}} - T_{\text{ret}}(k)\right), \tag{27}$$

where the heat supply of the heat pump $\dot{Q}_{\text{HP}}$ is expressed using the fluid's mass flow $\dot{m}_f$ from and to the building, the heat pump's efficiency η_{HP} and the specific heat of the fluid c_f. T_{sup} is the required supply temperature of the fluid which will be at the inlet of the building. This temperature is fixed to remain a constant temperature in the buildings' boiler.

2.2.2. Piping system

To accurately assess the heat losses in the pipe, a temperature profile is established that delineates how temperature varies along the pipe's length. This pipe, which is embedded underground, principally dissipates heat to the surrounding soil. Given that the pipe's temperature fluctuates along its length, the rate of heat transfer to the soil also varies correspondingly. To model this phenomenon, the following equations are introduced, employing dx to represent an infinitesimally small segment of the pipe

$$\dot{m}_f c_f dT_f = \dot{Q}_f = \dot{m}_f c_f \left[T_{\text{f}}^{\text{x}}(k) - T_{\text{f}}^{\text{x+dx}}(k)\right] \tag{28}$$

and

$$\dot{Q}_f = \frac{\left[T_{\text{f}}^{\text{x}}(k) - T_{\text{s}}(k)\right] dx}{R_t} \tag{29}$$

where $\dot{m}_f$ and c_f are the mass flow and specific heat of the fluid in the pipes. T_{f}^{x} is the temperature of the fluid at the inlet of pipe segment with length dx, and $T_{\text{f}}^{\text{x+dx}}$ is the outlet temperature of the segment. R_t is the total thermal resistance from the fluid to the grounds' surface. The length of the small segment of the pipe is dx and T_s is the temperature at the ground's surface.

A differential approach is employed to quantify the variation in heat exchange along the pipe's length, accounting for the changing temperature of the fluid inside the pipe as it loses heat to the surrounding soil. This method involves setting up an integral equation, where integration with respect to the fluid temperature change dT_f on the left-hand side is done, representing the thermal energy variation within the pipe, and with respect to the pipe segment length dx on the right-hand side, denoting the

spatial progression along the pipe, resulting in

$$\frac{dT_f}{T_{\mathrm{f}}^{\mathrm{x}}(k) - T_{\mathrm{s}}(k)} = \frac{dx}{\dot{m}_f c_f R_t}. \tag{30}$$

The integration boundaries are defined by the inlet and outlet fluid temperatures for the left-hand side, and the start and end points of the pipe's length for the right-hand side. This approach yields a comprehensive model that captures the dynamics of heat loss across the pipe, facilitating a precise determination of how the fluid temperature evolves from the point of entry to the point of exit [28], resulting in

$$\int_{T_{\mathrm{in}}}^{T_{\mathrm{out}}} \frac{dT_f}{T_{\mathrm{f}}^{\mathrm{x}}(k) - T_{\mathrm{s}}(k)} = \int_0^L \frac{1}{\dot{m}_f c_f R_t}\, dx. \tag{31}$$

A constant temperature over the area is assumed due to negligible district heating influence on ground surface temperature [33], thus

$$\frac{T_{\mathrm{s}}(k) - T_f^{\mathrm{out}}(k)}{T_{\mathrm{s}}(k) - T_f^{\mathrm{in}}(k)} = e^{-\frac{L}{\dot{m}_f c_f R_t}}. \tag{32}$$

Isolating T_f^{out} results in

$$T_f^{\mathrm{out}}(k) = T_{\mathrm{s}}(k) - \left[T_{\mathrm{s}}(k) - T_f^{\mathrm{in}}(k)\right] e^{-\frac{L}{\dot{m}_f c_f R_t}} \tag{33}$$

where T_f^{out} is the outlet temperature and T_f^{in} is the inlet temperature of the pipe, L is the length of the pipe. The total thermal resistance R_t is a combination of the conductive and convective heat transfer coefficients from the fluid to the ground.

To calculate the temperature at the grounds' surface, a method to model a temperature gradient over a depth y is used [21]. For modelling heat loss to the ground, the temperature at any specific depth y is assumed to be constant over the total area. The system is represented as a semi-infinite solid along one-dimensional coordinates to calculate the soil temperature. The boundary conditions for the model are surface temperature and the temperature at a point underground with a constant temperature. The first boundary, the surface temperature, can be obtained using Fourier's Conductivity Law, Newton's Law of Cooling, and Stefan–Boltzmann's Law of Radiation, resulting in

$$-k_{\mathrm{soil}} \frac{\Delta T_{\mathrm{soil}}(y,k)}{\Delta y} = h(k)\left[T_{\mathrm{amb}}(k) - T_{\mathrm{s}}(k)\right] - \epsilon \Delta R(k) + \alpha_0 G(k), \tag{34}$$

where $T_{\mathrm{s}}(y=0)$ is the temperature of the soil at the surface, k_{soil} is the thermal conductivity of the soil. ϵ is the thermal emissivity of the soil, α_0 is the soil's absorbtivity and G is the solar radiation. T_{amb} is the ambient temperature. ΔR is given with the following equation:

$$\Delta R(k) = \sigma\left[T_{\mathrm{s}}^4(k-1) - T_{\mathrm{sky}}^4(k)\right]. \tag{35}$$

Here, T_{sky} can be calculated using Brunt's model and $T_{\mathrm{s}}(k-1)$ is the surface temperature ate the previous time step. The total heat transfer coefficient h is a combination of the convective and radiative heat transfer coefficients, given by

$$h(k) = h^{\mathrm{conv}}(k) + h^{r}(k). \tag{36}$$

The radiative heat transfer coefficient h^{conv} is calculated with

$$h^{r}(k) = \epsilon\sigma\left[T_{\mathrm{s}}^2(k-1) + T_{\mathrm{sky}}^2(k)\right]\left[T_{\mathrm{s}}(k-1) + T_{\mathrm{sky}}(k)\right]. \tag{37}$$

Assuming that the temperature profile over y within the soil is linear, the following equation can be used

$$-k_{\mathrm{soil}} \frac{\Delta T_{\mathrm{soil}}(y,k)}{\Delta y} = -k_{\mathrm{soil}} \frac{T_{\mathrm{d}} - T_{\mathrm{s}}}{d} \tag{38}$$

where d is the distance of the surface to a point underground where the environmental effects are neglectable, this is considered at a depth of 6 m [24]. This temperature can be calculated with the following equation:

$$T_{\mathrm{d}} = 0.0318d + 8.01768 \tag{39}$$

The expression for the temperature at the surface is then

$$T_{\mathrm{s}}(k) = \frac{k_{\mathrm{soil}} T_{\mathrm{d}} + dhT_{\mathrm{amb}}(k) - d\varepsilon\Delta R(k) + d\alpha_o G(k)}{dh + k_{\mathrm{soil}}} \tag{40}$$

To quantify the heat loss to the ground, a theory from Wallenten [34] is applied, which focuses on the heat conduction dynamics of an insulated pipe embedded in the ground. The conductive heat transfer resistance of the pipe $h_{\mathrm{f-s}}^{\mathrm{cond}}$ can be calculated using [34]

$$\frac{1}{h_{\mathrm{f-s}}^{\mathrm{cond}}} = \ln\left(\frac{2H}{r_o}\right) + \beta. \tag{41}$$

The distance between the centre of the pipe and the ground is H. The thickness of the insulation of the pipe is expressed with an inside radius r_i and an outside radius r_o. The dimensionless parameter β is expressed with the following equation. The error, using

this formula for $h_{\mathrm{p-g}}^{\mathrm{cond}}$, is typically less than 0.5% [34].

$$\beta = \frac{\kappa_g}{\kappa_t} \ln\left(\frac{r_o}{r_i}\right) \tag{42}$$

The thermal conductivity of the tube is κ_t, and the thermal conductivity of the ground is κ_g. This equation is designed for a single-layer tube embedded in the ground. However, the district heating network employs a pipe that features an inner tube encased by an additional layer of insulation. Therefore, the dimensionless parameter needs to be adapted to accommodate this multi-layered structure as follows

$$\beta = \frac{\kappa_g}{\kappa_t} \ln\left(\frac{r_{i-o}}{r_i}\right) + \frac{\kappa_g}{\kappa_i} \ln\left(\frac{r_o}{r_{i-o}}\right) \tag{43}$$

where the thermal conductivity of the insulation is κ_i and r_{i-o} is the outer diameter of the tube which is the inner diameter of the insulation. The total heat transfer coefficient can be translated to a total heat resistance

$$R_t = R_{\mathrm{cond}} + R_{\mathrm{conv}} \tag{44}$$

$$R_{\mathrm{cond}} = \frac{\ln\left(\frac{2H}{r_o}\right)}{2\pi\kappa_g} + \frac{\ln\left(\frac{r_{i-o}}{r_i}\right)}{2\pi\kappa_t} + \frac{\ln\left(\frac{r_o}{r_{i-o}}\right)}{2\pi\kappa_i} \tag{45}$$

Finally, the total heat loss of the pipe can be calculated using the inlet and outlet temperature of the fluid in the pipe.

$$\dot{Q}_{\mathrm{pipe}} = \dot{m}_{\mathrm{f}} c_{\mathrm{f}} \left[T_{\mathrm{f}}^{\mathrm{out}}(k) - T_{\mathrm{f}}^{\mathrm{in}}(k)\right]. \tag{46}$$

2.3. Thermal demand

The thermal demand for buildings $\dot{Q}_{\mathrm{D}}$ primarily stems from maintaining a consistent indoor temperature. Heat losses to the environment result in a temperature decline within these buildings. To counteract this effect and keep the temperature stable, it is necessary to supply an amount of heat equivalent to the thermal losses. The buildings are considered with losses to the environment through walls, double-glass windows and the roof, and due to ventilation and infiltration. Using the model proposed in [21], we estimated the thermal demand on the building; however, the model does not account for building occupants, appliances or radiative heat through the windows. With respect to the latter, since this work focuses on heating, neglecting the radiative heat will result in a conservative approach, as it would reduce the thermal demand (depending on the size, orientation and materials of the windows).

Assuming no mass exchange between the house's exterior and interior, the change in the indoor temperature ΔT during a time step Δt can be calculated as a function of the building's thermal mass and specific heat m and c, and the sum of thermal powers $\dot{Q}_i$ with

$$\frac{\Delta T}{\Delta t} \sum_{i=1}^{n} m_i c_i = \sum_{i=1}^{n} \dot{Q}_i. \tag{47}$$

Considering a single input of heat into the building and considering a heat demand equivalent to the heat losses, (47) can be rewritten as

$$\frac{\Delta T_{\mathrm{in}}}{\Delta t} \sum_{i=1}^{n} m_i c_i = \dot{Q}_{\mathrm{in}} - \dot{Q}_{\mathrm{D}}. \tag{48}$$

Each building is heated by its own individual heat pump. The pump supplies a constant temperature supply into the building T_{sup}, to remain a constant temperature of the indoor boiler equal to the supply temperature. Isolating the indoor temperature results in

$$T_{\mathrm{in}}(k+1) = T_{\mathrm{in}}(k) + \frac{\Delta t(\dot{Q}_{\mathrm{HP}} - \dot{Q}_{\mathrm{D}})}{\sum_{i=1}^{n} m_i c_i} \tag{49}$$

where the heat inserted into the building is provided by the heat pump $\dot{Q}_{\mathrm{HP}}$, and ΔT_{in} is the change in temperature during time step Δt.

To analyse the building heat loss, it is conceptualised as one space with its thermal mass and losses to the external environment. Heat transfers to the ground and radiative heat transfers are not considered in this model. The heat loss from the building primarily results from the unique characteristics of the walls, windows, and roof that interface with the environment. These losses are conductive and convective heat transfers and additionally ventilation and air infiltration losses, using a method described by [21], the convective losses are modelled by dividing them into two identical sections, each spanning half the original distance, with the thermal mass positioned in between. The overall heat transfer coefficient, which quantifies these losses, is shown in Fig. 3 and can be calculated using

$$U = \left(\sum_{i=1}^{n} \frac{1}{h_i} + \sum_{i=1}^{m} \frac{L_i}{k_i}\right)^{-1}, \tag{50}$$

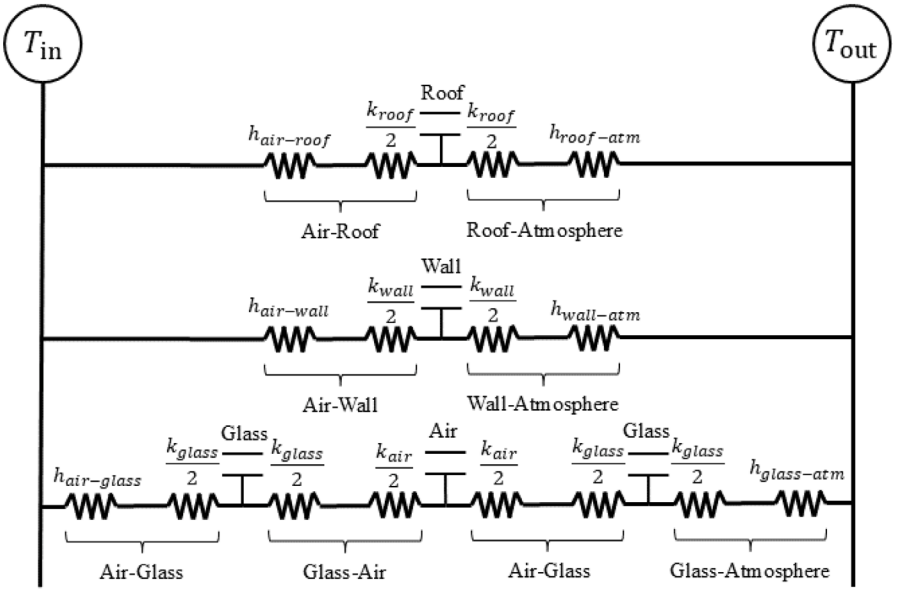

Fig. 3. Convective and conductive thermal losses through the roof, walls, and windows considered per house room [21].

where h_i are the convective heat transfer coefficients, k_i is the materials' conductivity and L_i the thickness of the conductive materials. Using this heat transfer coefficient, the heat losses from the building through conduction and convection can be determined as

$$\dot{Q}_{\mathrm{L}} = \sum_{i=1}^{n} U_i A_i \Delta T. \tag{51}$$

Here, A_i are the surface areas with the corresponding heat transfer coefficients, and ΔT denotes the temperature difference between the indoor and outdoor environments.

The ventilation and infiltration heat exchange is calculated through the method suggested by the American Society of Heating, Refrigerating and Air-Conditioning Engineers (ASHRAE) [28]. This heat exchange results from the mass exchange of air entering and exiting the house. The ventilation heat exchange is described as

$$\dot{Q}_{\mathrm{v}} = c_a \rho_a q_v \Delta T, \tag{52}$$

where, c_a and ρ_a are the specific heat capacity and density of air, ΔT is the temperature difference between the outside and inside of the building. The ventilation airflow, denoted as q_v can be calculated using

$$q_v = 0.03 A_{\mathrm{cf}} + 7.5\left(N_{\mathrm{br}} + 1\right), \tag{53}$$

where, A_{cf} is the conditioned area of the building and N_{br} is the number of bedrooms. Next, the infiltration heat exchange is described as

$$\dot{Q}_{\mathrm{i}} = c_a \rho_a q_i \Delta T \tag{54}$$

where the infiltration airflow, denoted as q_v can be calculated using

$$q_i = A_{\mathrm{ex}} A_l \sqrt{C_s \left|\Delta T\left(k\right)\right| + C_w u^2}, . \tag{55}$$

The exposed area is represented as A_{es} and the leakage area as A_l. The stacking coefficient C_s depends on the number of floors, while the wind coefficient C_w depends on the building's surroundings [28], and u is the wind speed. Finally, the total heat demand of the buildings is the sum of the losses due to conduction and convection $\dot{Q}_{\mathrm{L}}$, ventilation $\dot{Q}_{\mathrm{v}}$ and infiltration $\dot{Q}_{\mathrm{i}}$ losses, given by

$$\dot{Q}_D = \dot{Q}_{\mathrm{L}} + \dot{Q}_{\mathrm{v}} + \dot{Q}_{\mathrm{i}}. \tag{56}$$

2.4. Thermal network

The previous systems are connected to form a 5GDHN. The entry and exit temperature points for each component form the basis of the systems' dynamics. Here, the outlet temperature for one component is assumed becoming the inlet temperature for the other in a sequential manner. The system's initial setup features a centralised PVT and ATES system configuration. All components are

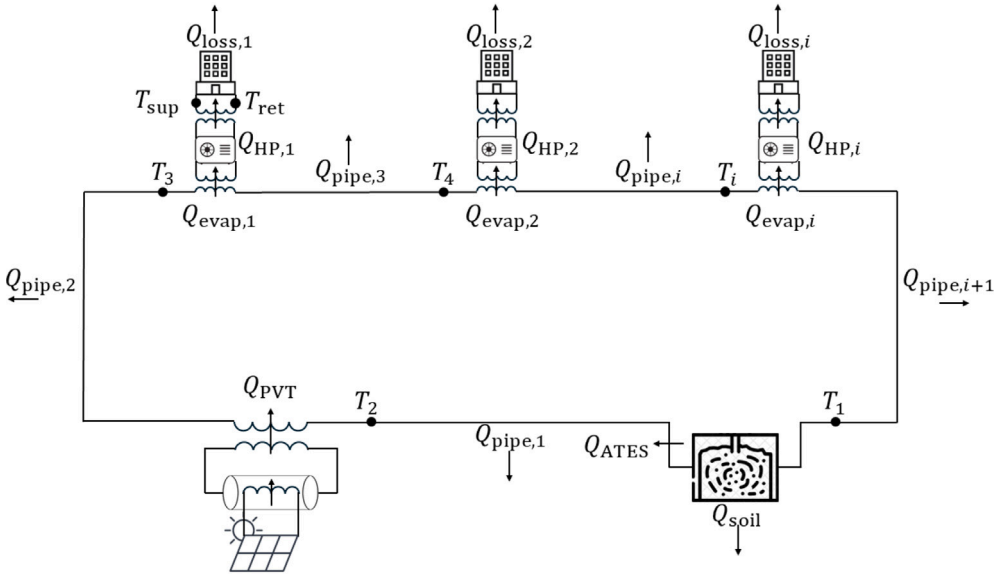

Fig. 4. Thermal network configuration.

interconnected through pipes except for the heat pumps to the corresponding buildings. This network is designed in such a way that it is a closed loop, and the carrier thermal fluid circulates clockwise through all the heat pumps once it has passed through the PVT and the ATES system. The thermal connection to the heat pumps, buildings and PVT are done through a heat exchanger. On the other hand, for the ATES and pipes, the components are directly connected to the thermal carrier. The schematic overview of the system can be seen in Fig. 4. The number of buildings with heat pumps is in reality higher, and is therefore expressed as the ith building, heat pump or pipe.

The temperatures at the different points in the thermal network are calculated using the previous temperature and the characteristic heat exchange of the component. Due to multiple buildings with corresponding heat pumps and pipes connecting them, a set of equations is formed for each ith combination of these components. The temperatures of the connection between the buildings and the heat pumps can be calculated using

$$\dot{Q}_{\text{building}} = \frac{\sum_{i=1}^{n} m_i c_i \left[T_{\text{in}}(k-1) - T_{\text{in}}(k-2)\right]}{\Delta t} - \dot{Q}_{\text{D}} \tag{57}$$

with

$$T_{\text{sup}}(k) = T_{\text{ret}}(k-1) + \frac{\dot{Q}_{\text{building}}(k)}{\dot{m}_{fb} c_f} \tag{58}$$

and

$$T_{\text{ret}}(k) = T_{\text{ret}}(k-1) + \frac{\dot{Q}_{\text{building}}(k-1) + \dot{Q}_{\text{HP}}(k-1)}{\dot{m}_{fb} c_f}, \tag{59}$$

where the T_{sup} is the supply temperature into the building which is heated up to 53 °C when the T_{ret} out of the building drops below 50 °C, T_{in} is the inside temperature of the building. The water mass flow in and out of the building is $\dot{m}_{fb}$. The following equations connect the heat pumps with their subsequent pipes.

$$T^{\text{out}}_{\text{HP,i}}(k) = T^{\text{in}}_{\text{HP,i}}(k-1) - \frac{Q_{\text{evap,i}}(k)}{\dot{m}_f c_f}, \tag{60}$$

$$T^{\text{out}}_{\text{pipe,i}}(k) = T^{\text{in}}_{\text{HP,i}}(k-1) - \frac{\dot{Q}_{\text{evap,i}}(k) + \dot{Q}_{\text{pipe,i}}(k-1)}{\dot{m}_f c_f}, \tag{61}$$

$$T^{\text{in}}_{\text{HP,i+1}}(k) = T^{\text{out}}_{\text{pipe,i}}(k) \tag{62}$$

Considering a centralised PVT and ATES, the following equations express the total systems' thermodynamics.

$$T^{\text{out}}_{\text{PVT}}(k) = T^{\text{in}}_{\text{ATES}}(k-1) - \frac{\sum_{i=1}^{n} \dot{Q}_{\text{evap,i}}(k) + \sum_{i=2}^{n} \dot{Q}_{\text{pipe,i}}(k)}{\dot{m}_f c_f}, \tag{63}$$

$$T^{\text{in}}_{\text{PVT}}(k) = T^{\text{in}}_{\text{ATES}}(k-1) + \frac{\dot{Q}_{\text{PVT}} - \sum_{i=1}^{n} \dot{Q}_{\text{evap}}(k) - \sum_{i=2}^{n} \dot{Q}_{\text{pipe,i}}(k)}{\dot{m}_f c_f}, \tag{64}$$

Fig. 5. Map of the heating network in Hilversum Werf, indicating the location of the centralised ATES.

Table 3
Parameters of the centralised ATES.

Parameter	Symbol	Value	Units
Radius ATES	R	250	m
Height ATES	d	10	m
Number of PVT	n	800	–
Length pipe 16	L	70	m
Length pipe 17	L	100	m

$$T_{\mathrm{ATES}}^{\mathrm{in}}(k) = T_{\mathrm{ATES}}^{\mathrm{in}}(k-1) + \frac{\dot{Q}_{\mathrm{PVT}} - \dot{Q}_{\mathrm{ATES}} - \sum_{i=1}^{n} \dot{Q}_{\mathrm{evap}}(k) - \sum_{i=1}^{n} \dot{Q}_{\mathrm{pipe,i}}(k)}{\dot{m}_f c_f}. \tag{65}$$

The district heating thermal network connects the centralised PVT and the ATES to the buildings' thermal network through the water-to-water heat pump heat exchangers. While the PVT supplies thermal power to the district network, the heat pumps demand thermal power from the district network to heat the buildings through the building thermal network. The strategy used to control the heat flow is similar to the one used in [21]. On the one hand, every building measures the indoor temperature every 15 min and compared with a desired setpoint temperature. If the measured temperature is below the setpoint, the building's heat pump is activated, keeping the fluid in the building's network between 50 ° C and 53 ° C. On the other hand, the PVT operation involves a tank temporarily storing thermal energy. The PVT modules heat the water in the tank, and this tank transfers the heat to the district heating network. The tank exchanges heat with the district heating network only if its temperature exceeds the network's. This design ensures that the PVT modules never cool down the network, as the tank will not transfer heat to the network unless it has a higher temperature. This approach optimises heat management, ensuring efficient and effective heating within the system.

3. Network configuration

The base case uses a single ATES, as shown in Fig. 5. The radius of the ATES is depicted as a red line, with the centre marked by a red dot. The ATES is considered a circle with a specific radius and height. The aquifer consists of water and sand, with the water assumed to be perfectly mixed within the sand of the aquifer. The input and output of the aquifer are visualised using pipes with lengths L16 and L17. The initial amount of PVT modules is based on Hilversum's plans to install 800 solar modules on the carport roof. The parameters are summarised in Table 3.

The second scenario, illustrated in Fig. 6, involves implementing multiple ATES systems within the base case of the Hilversum district heating network. The locations for these ATES systems are strategically selected to ensure an equal distribution of buildings between each aquifer and to prevent overlap between the aquifers. The sizes of the individual ATES systems are designed so that

Fig. 6. Map of the heating network in Hilversum Werf, indicating the possible location of the distributed ATES.

Table 4
Parameters of the distributed ATES.

Parameter	Symbol	Value	Units
Radius ATES	R	144	m
Height ATES	d	10	m
Number of PVT	n	800	–
Length pipe 16	L	70	m
Length pipe 17	L	100	m
Length pipe 18	L	80	m
Length pipe 19	L	110	m
Length pipe 20	L	80	m
Length pipe 21	L	80	m

their combined total volume matches that of a centralised system utilising a single aquifer. To integrate these ATES systems into the existing district heating network, additional pipes are installed while all other parameters remain unchanged (see Table 4).

In both cases (centralised and distributed), the highest temperatures in the distribution network are recorded immediately after the PVT, where the water has just been heated. The large temperature fluctuations are due to the daily variations between day and night. In the centralised case, the temperature of the water exiting the ATES remains the most stable, reflecting the internal temperature of the ATES, which gets colder while circulating in the network, reaching its coldest point when entering the ATES, as heat has been extracted by the heat pumps to warm the buildings. In the distributed case, however, having multiple ATES distributed throughout the network keeps the water temperature higher, as the thermal inertial of the ATES prevents it from dropping considerably, increasing the heat pump's COPs. Table 5 summarises the total heat transfer over the year for all components for both scenarios. The higher temperature in the district heating network, in the distributed case, entails slightly less thermal power from the PVT, given the higher inlet temperature, but also increases considerably the losses in the ATES and the distribution network, as the temperature difference between the fluid and its surroundings is higher. In addition, the total annual power supply and usage per component, including the exchange with the grid, are summarised in Table 6. As mentioned, the distributed case requires less electric power to operate the heat pumps thanks to the higher temperature in the networks; however, having multiple ATES increases the hydraulic power required to operate the system as many times as the number of ATES, for this reason, the net grid exchange increases threefold.

4. Sizing

The sizes of the PVT and ATES components will be analysed for a centralised system, as recommended in Section 3. Considering that a larger PVT system reduces the net electrical consumption of the overall district heating network while increasing the network temperature, thus, increasing the COP, we expected that the optimal PVT size would be close to the maximum possible size given

Table 5
Total heat transfer per component.

Component	Symbol	Centralised ATES [MWh]	Distributed ATES [MWh]
PVT	Q_{PVT}	2 504	2 408
Losses buildings	Q_{loss}	−1 410	−1 410
Evaporator HP	Q_{evap}	−956	−969
Heat ATES loss	$Q_{ATES,loss}$	−277	−664
Heat pipe loss	$Q_{pipe,loss}$	−3.52	−4.90

Table 6
Total electrical energy transfer per component.

Component	Symbol	Centralised ATES [MWh]	Distributed ATES [MWh]
PVT	E_{PVT}	394	394
Load buildings	E_{load}	−1 120	−1 119
Heat pump	E_{HP}	−453	−440
ATES pump	E_{ATEP}	−806	−2 417
Shortage grid	$E_{grid,shortage}$	−2 023	−3 583
Surplus grid	$E_{grid,surplus}$	38	0
Net grid	E_{grid}	−1 985	3 583

Table 7
Total heat transfer per component for different sizes.

Variable	R100/n600	R100/n800	R200/n600	R200/n800	R300/n600	R300/n800
Q_{PVT} [MWh]	2 244	2 247	2 465	2 469	2 518	2 523
Q_{evap} [MWh]	−976	−976	−959	−959	−954	−954
$Q_{ATES,loss}$ [MWh]	−244	−244	−272	−273	−279	−280
$Q_{pipe,loss}$ [MWh]	−7.46	−7.47	−3.98	−3.99	−3.25	−3.26

Table 8
Total electrical energy transfer per component for different sizes.

Variable	R100/n600	R100/n800	R200/n600	R200/n800	R300/n600	R300/n800
E_{PVT} [MWh]	292	394	295	394	295	394
E_{HP} [MWh]	−433	−433	−450	−450	−455	−455
$E_{grid,shortage}$ [MWh]	−2 075	−2 004	−2 091	−2 021	−2 096	−2 025
$E_{grid,surplus}$ [MWh]	11	38	11	38	11	38
E_{grid} [MWh]	−2 064	−1 965	−2 081	−1 982	−2 085	−1 987

the space constraints, 800 modules. Therefore, we limited the PVT size range between 600 to 800 modules. On the other hand, we evaluated ATES radii between 100 and 300. Table 7 provides a result summary of some of the combinations, where the nomenclature R*i*/n*j* indicates a radius *i* in metres and *j* is the number of modules.

As shown in Table 7, increasing the size of the PVT system consistently results in higher heat and electricity production, thereby enhancing overall system thermal and electric performances without any additional downsides as expected. Conversely, reducing the size of the ATES leads to a warmer network, which decreases the power consumption of heat pumps due to a higher COP. However, it also causes more temperature divergence within the system, increasing losses in the ATES and pipes and decreasing the heat the PVT provides. A warmer network reduces heat pump power consumption, which is the only power variable affected by the dimensions of the ATES. Consequently, a smaller ATES results in lower net power use. The net grid exchange is considered the best result for monitoring system performance. An overview of the different dimensions and resulting net grid exchange is shown in Table 8. As expected, larger PVT systems consume less energy from the grid but also entail a higher surplus of energy injected due to the mismatch between the pump consumption and the PVT generation. From the ATES perspective, smaller volumes require less power to operate as the temperature in the water is higher. The higher temperature in the network increases the buildings' heat pump COP, reducing the energy consumption to meet the same thermal demand.

Smaller ATES have more variability in the water temperature throughout the year. After one year of simulation, each size's final ATES temperature differed from the starting 11 ° C, meaning that the system does not reach a thermal balance between thermal input from the PVT, the thermal demand and losses in one year. We, therefore, extended the simulation until the temperature difference between the first and last simulation time step per year was below 1 ° C. The temperatures of smaller ATES systems are higher and exhibit greater temperature divergence throughout the seasons since the results are influenced by weather conditions, which can vary annually. The steady-state temperatures for different ATES sizes are shown in Fig. 7. The corresponding yearly net grid exchanges are summarised in Table 9. A smaller ATES can heat up more, increasing the heat pump's COP, but the temperatures fluctuate more throughout the seasons. This indicates a much larger weather dependency on the overall stability of the aquifer temperatures. An aquifer that is too small can lead to too extreme temperatures.

The sizing analysis has given the following results. Increasing the number of PVT modules to the maximum of 800 enhances electrical and thermal generation, thereby improving overall system performance without direct drawbacks. A larger ATES unit helps

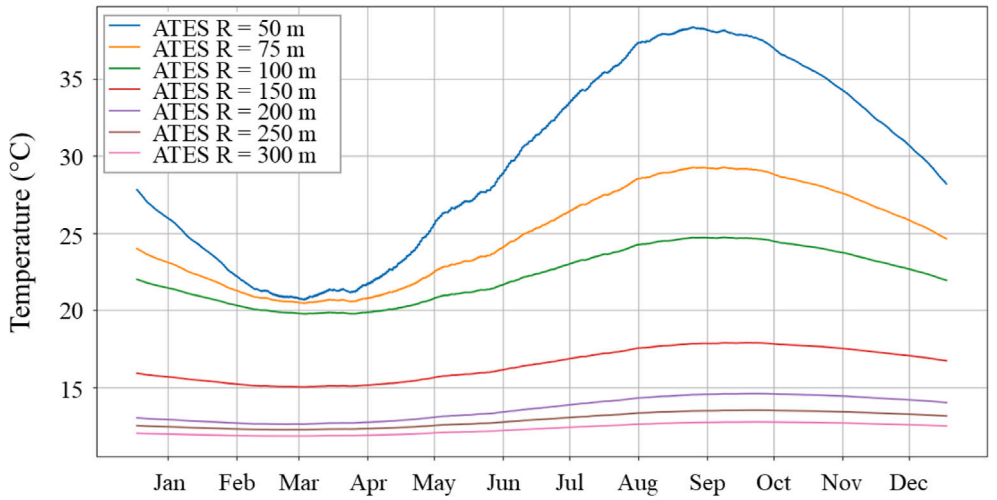

Fig. 7. Temperatures ATES at steady state, 15-minute time step.

Table 9
Yearly net grid exchange during steady state for different ATES radii.

ATES R [m]	n modules	T_0 [° C]	Net grid [MWh]
35	800	27.4	−1928
50	800	27.8	−1923
75	800	24.0	−1922
100	800	22.0	−1924
125	800	18.0	−1931
150	800	15.9	−1942
200	800	13.0	−1966
250	800	12.5	−1973
300	800	12.0	−1978

maintain a more stable temperature gradient throughout the year, though it operates at lower temperatures, whereas smaller volume aquifers experience greater temperature fluctuations. The variable net power consumption depends primarily on the heat pumps and their corresponding COP. Due to the maximum operational COP of the heat pumps (3.6), an optimal boundary temperature exists, around 19.5 °C, at which they function most efficiently. Thus, the objective is to maintain the inlet temperature (T_{in}) for each heat pump as close to this optimal temperature as possible across all seasons. Operating at higher temperatures results in increased heat losses. Therefore, a balance must be struck between maintaining the correct operating temperature, minimising heat losses, and managing seasonal temperature fluctuations.

To minimise CO_2 emissions, we quantified the system's installation and operational phases in equivalent CO_2. For operational CO_2 emissions, we used data from Nowtricity [35], which provides monthly average grams of CO_2 equivalent per kWh for power generated in the Netherlands. Then, the carbon emissions for the variable component installation must be determined. This data allows quantifying the CO_2 emissions associated with the variable components PVT and ATES. On the one hand, the carbon emissions for the PVT primarily depend on the emissions resulting from the manufacturing of the modules. Estimations for PV modules, expressed in grams of CO_2 equivalent, consider the entire lifecycle, including manufacturing and electricity generation. According to a study by Virtuani [36], the CO_2 emissions for PV modules in the Netherlands, considering the local climate, are estimated at 40.1 g CO_2eq/kWh for optimally tilted modules. Since this intensity factor pertains only to the PV part of the PVT, it will be multiplied by the electricity generation of the PVT to quantify its carbon emissions. On the other hand, the installation emissions of the ATES are challenging to quantify, scaled to the aquifer's size. Research into the ATES emissions shows that they largely depend on the system's operation [37]. However, a case study in the Netherlands has documented the amount of diesel used for constructing an ATES well, which is determined to be 3 250 L [37]. Using the CO_2 emission factor of 2.68 kg/L for diesel, constructing an ATES well results in 8 710 kg of CO_2 emissions. Over an estimated lifetime of 30 years, this annual CO_2 emission is negligible for the optimisation problem.

The total CO_2 emissions will include both the operational emissions of the system and the installation emissions of the PVT modules. The installation emissions of the ATES are excluded as they are considered negligible. The equation for the total emissions is expressed as

$$\text{CO}_2 e_{\text{total}}(n, R) = \text{CO}_{\text{op}}(n, R, T_0) + \text{CO}_{\text{inst}}(n, R, T_0) \tag{66}$$

with

$$\text{CO}_2 e_{\text{op}}(n, R) = a P_{\text{G}}(n, R, T_0), \tag{67}$$

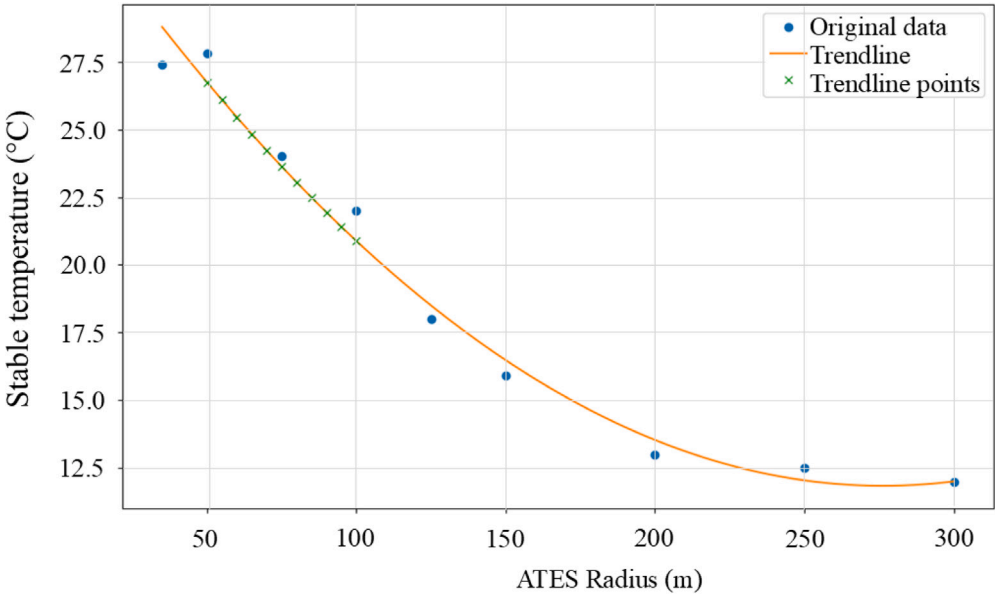

Fig. 8. Operating temperature trendline for different ATES radii.

and

$$CO_2e_{inst}(n) = bP_{PV}(n, R, T_0). \tag{68}$$

Here, CO_2e_{total} represents the total CO_2 emissions, CO_2e_{op} the operational CO_2 emissions, and CO_2e_{inst} is the installation CO_2 emissions. The variables n and R correspond to the number of PVT modules and the ATES radius, respectively. The initial operational temperature of each ATES size is expressed as T_0. The kg CO_2 equivalent per kWh of grid consumption is expressed as a, and the kg CO_2 equivalent per kWh of PV generation is expressed as b, set at 40.1 g CO_2eq/kWh. P_G and P_{PV} represent the power consumption from the grid and the power generation by the PVT modules, respectively.

The constraints for the variables in the optimisation function include the number of PVT modules (n) and the ATES volume. The sizing analysis showed that increasing the number of solar modules to the maximum enhances the system's performance, with the carport's maximum capacity being 800 modules. To assess the significance of installation emissions, a range of 700 to 800 modules is chosen for analysis. For the ATES size, expressed as the radius R, it has been shown that net power grid consumption is lowest for an ATES radius of 75 m. Similarly, low net grid power consumption results were observed for ATES radii of 50 m and 100 m. Therefore, the CO_2 emissions will be analysed for ATES radii between 50 m and 100 m. The solution to the problem will be calculated discretely. The resolution will be set at 10 PVT modules and 5 m for the ATES radius. The optimisation problem is formulated in (66) results in

$$\begin{aligned} \min_{n,R} \quad & CO_2e_{total}(n, R, T_0) \\ s.t. \quad & 700 \leq n \leq 800 \\ & 50 \leq R \leq 100 \end{aligned} \tag{69}$$

As the radii of the ATES will change to solve the problem, a specific initial operational temperature for each ATES size needs to be determined, as discussed previously. Using the stable-state values determined, the intermediate points were interpolated using a polynomial approximation, as shown in Fig. 8.

In addition, [38] mentions that ATES systems can affect the subsurface, i.e., the injected water cannot be too hot. The maximum injection temperature in the ATES can range from 25 ° C to 30 ° C. Fig. 9 shows the configurations that exceed the threshold temperature, with one case at 30 ° C and the other at 25 ° C. The configurations exceeding the maximum temperature have a shade of grey. It is clear that the optimal solution for minimising CO_2 emissions is achieved with the maximum number of PVT modules, which is 800. This indicates that the operational CO_2 emissions of the entire system are more significant than the installation emissions of the PVT modules. The configuration with the lowest CO_2 emissions features a 60 m ATES and 800 solar modules. However, the difference between this and other configurations is minimal; a deviation of 5 m from the 60 m ATES radius results in only a 10 kg CO_2 equivalent change.

Fig. 10 presents the optimisation problem results. The amount of CO_2 equivalent decreases as the ATES size approaches its maximum temperature threshold. The two threshold values, maximum 30 ° C and 25 ° C, are indicated by red lines. The minimum

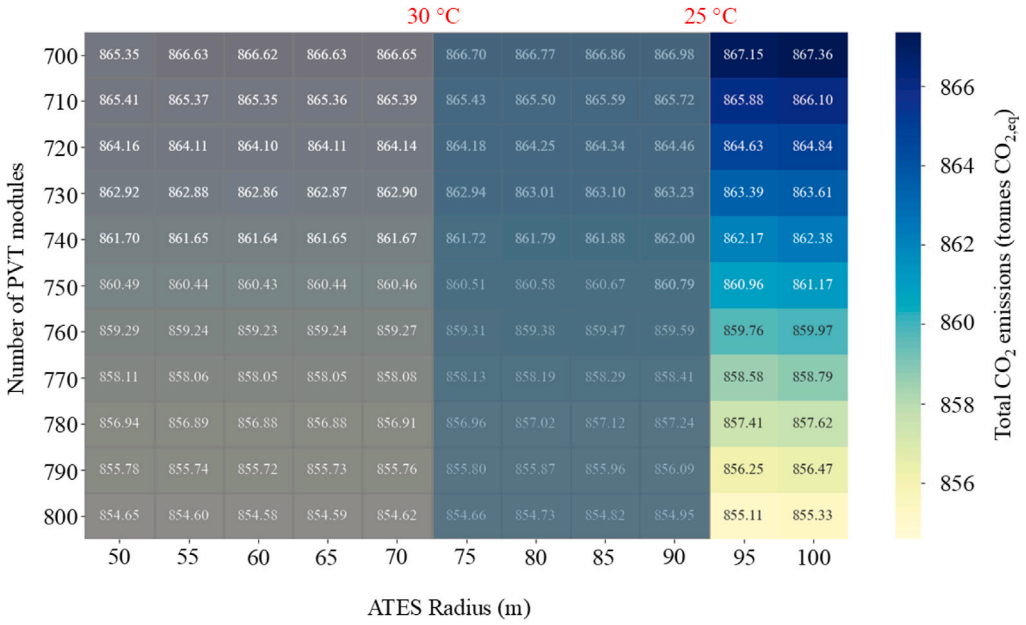

Fig. 9. Total CO_2 Emissions with 25 ° C and 30 ° C thresholds.

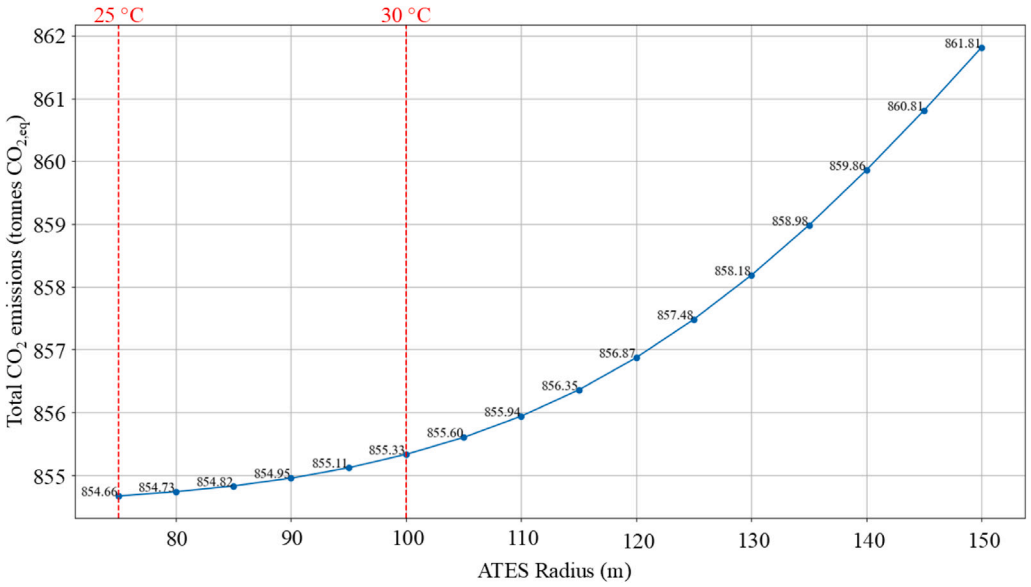

Fig. 10. Total CO_2 Emissions with 800 PVT modules and maximum temperature threshold.

CO_2 equivalent for both cases occurs precisely at these specific thresholds. Additionally, the data reveals that the deviation of CO_2 equivalent increases with the ATES size, indicating an exponential relationship between the ATES size and the CO_2 equivalent. The difference in CO_2 equivalent between the smallest ATES sizes, R = 75 m and R = 80 m, is merely 80 kg. In contrast, the difference between the largest ATES sizes, R = 145 m and R = 150 m, is as much as a ton of CO_2 equivalent.

The optimisation analysis suggests that the CO_2 emissions caused by the PVT installation are significantly lower than those resulting from grid electricity purchases, leading to optimal solutions at the maximum number of PVT modules. The minimal CO_2 emission solutions can be found at the maximum temperature thresholds for this system. For the optimal aquifer size regarding just CO_2 emissions, the temperatures become too high regarding the maximum temperatures. Additionally, CO_2 emissions remain low within this range of aquifer sizes near the maximum temperature thresholds, resulting in only minor differences between the 30 ° C and 25 ° C boundaries, indicating low significance in the results at these temperature borders.

Table 10
Network configuration results summary.

Metric	Centralised	Distributed
ATES thermal losses	Fewer losses due to lower temperatures.	Higher losses due to higher temperatures.
Network thermal losses	Fewer losses due to lower temperatures.	Higher losses due to higher temperatures.
Heat pump electric consumption	Lower temperature lead to lower COP and, therefore, higher consumption.	Higher temperature improves the COP, reducing energy consumption.
ATES pumping electric consumption	Less energy as its only one pumping system.	Higher energy consumption as there is one pumping system per ATES.
Grid exchange	Only one ATES pumping system reduces considerably the 5GDHN overall energy consumption.	The improvement in COP does not compensate for the consumption of multiple ATES pumping systems, leading to higher overall consumption.

5. Discussion

In Section 3, we compared a centralised and a distributed ATES configuration throughout the network, maintaining the total storage volume. From a capacity perspective, one could consider that having the same available storage, from an energy perspective, provides no difference. However, the thermal inertia of the ATES minimises the change in the network temperature; thus, having several ATES distributed in the network results in a more uniform network temperature. This is particularly beneficial to ensure a more even operation of the heat pumps connected to the distribution network since the COP depends on the network temperature, as shown in Eq. (25). In the case of a centralised ATES, the heat pumps connected closer to the ATES would have higher network temperatures than those connected towards the end of the circuit, thus, higher COPs. This is shown in Table 6, where the energy consumed by the heat pumps in the distributed case is around 3 % less than in the centralised case.

From a deployment and operative perspective, multiple ATES results are less attractive, in particular, given the small improvement in energy consumption. Multiple ATES require multiple installations, including not only major capital expenses but, most likely, more complex paperwork for permission from the local authorities. Similarly, each ATES require its circulation pump, increasing the energy consumption by a factor equal to the number of ATES. This is because the ATES would be located at similar depths, and the flow must remain. This is also confirmed in Table 6, where the ATES pump energy consumption is three times higher in the distributed case since it has three ATES. This entails a less favourable situation from an energy or cost perspective. Thus, the selection of a centralised configuration is deemed the best. This is consistent with the work presented by [13], where all the case studies studied had a single ATES in the heating network.

The study in Section 4 then provided insight into the optimal sizes for the PVT and ATES. With respect to the former, it was mentioned that larger PVT systems would be preferred. This was confirmed both from a thermal perspective in Table 7 and from an electric perspective in Table 8. In both cases, a larger PVT system entails more energy production; more thermal energy production increases the network temperature and, therefore, the COP of the buildings, whereas higher electric production minimises the net energy consumption from the grid to operate the circulation pumps. Those improvements are reflected in lower CO_2 emissions. As shown in Fig. 9, for every ATES radius, the higher the number of PVT modules, the lower the emissions, changing up to 12 tonnes of $CO_{2,eq}$ per year between systems with 700 and 800 modules.

Despite the size of the PVT system affecting the temperature of the ATES and the thermal network, the size of the ATES had a larger impact on the network temperature. This is explained by the fact that the ATES stores the surplus of thermal energy from the PVT; therefore, for a fixed PVT size, smaller ATES would increase their temperature faster. However, smaller capacity also entails faster drops in temperature, resulting in more notorious seasonal patterns, as shown in Fig. 7. Still, albeit more unstable, the average temperature in the ATES was higher for smaller capacities, which, as mentioned before, is preferred to increase the performance of the heat pumps. Our results suggest that temperatures above the limit of 25 ° C would result in lower equivalent CO_2 emissions, aligning with the results reported by [11,12]. Nonetheless, for the current limitations in available size for the PVT and maximum allowed ATES temperature, it was concluded that the optimal size combination of the PVT and ATES is 800 modules and a radius of 95 m. Tables 10 and 11 provide a summary of the results of this work in alignment with the metrics indicated in the contributions.

6. Conclusions

This research described an analytical model for a multi-carrier energy system case scenario in Hilversum, the Netherlands, utilising heat pumps, PVT, and ATES. The primary goal was to minimise CO_2 emissions by optimising the grid exchange resulting from the system's performance. Multiple configurations and a distribution scenario are analysed to determine optimal component sizes. Our main conclusions are as follows:

Table 11
Sizing results summary.

Metric	PVT size	ATES size
ATES thermal losses	Larger PVT systems provide more thermal power, increasing the ATES temperature and thermal losses.	Increased ATES size increases the losses given the larger contact area with the soil.
Network thermal losses	Larger PVT systems increase the overall network temperature, increasing the thermal losses.	Larger ATES work in lower temperatures, decreasing the thermal losses in the network.
Heat pump electric consumption	The size of the PVT do not affect the HP electrical consumption considerably.	A larger ATES decreases the network working temperature and, therefore, the COP, increasing the electric consumption.
Grid exchange	Larger PVT systems generate more electric energy, reducing the overall energy required from the grid.	Larger ATES reduce the network temperature, increasing the HP energy consumption.
Equivalent CO_2 emissions	Larger PVT systems reduce the energy required from the grid, decreasing the overall $CO_{2,eq}$ produced by the system operation.	Larger ATES increase the overall $CO_{2,eq}$ produced by the system operation due to the reduced heat pumps' COP.

- Distributed ATES maintained higher temperatures within the district heating network than the centralised case with the same ATES volume, resulting in higher temperatures as input for the heat pumps, enhancing their COP. However, the energy consumption of the additional ATES pumps and the higher thermal losses make the COP improvement neglectable. For the case study, choosing a distributed ATES configuration instead of a centralised increased the ATES losses 140 %, the distribution losses 39 %, and the circulation pumps energy consumption changed from a net injection of 1985 MWh to a net consumption of 3583 MWh.
- The layout of the piping network was deemed insignificant, as the heat loss in the pipes was relatively minimal and did not necessitate optimisation for distance, i.e., the losses in the piping are neglectable in comparison with the ATES, so the effect of the layout can be neglected. For our case scenario, the losses in the piping represent between 0.74% and 1.3% of the losses in the ATES for the distributed and centralised configuration, respectively.
- As the number of PVT modules increases, the system temperature rises, improving the system's overall performance, as more thermal energy is injected into the ATES.
- The size of the ATES system influences the magnitude and variability of temperature throughout the year. When the temperature divergence in the ATES is relatively high, it is largely due to the significant impact of the district heating network, which is more noticeable in smaller ATES systems. These smaller systems experience greater seasonal temperature fluctuations. Consequently, smaller ATES systems operate at higher temperatures overall, increasing heat losses to the surrounding soil, which remains at approximately 11 ° C. For the case study, a centralised ATES of 50 m radius has a yearly variation of almost 15 ° C, whereas an ATES with a radius of 150 m or more has seasonal variations below 3 ° C.
- Over time, the temperature within the ATES converges to an equilibrium point, balancing the heat input from the district heating network with the heat losses to the soil. Larger ATES systems, operating at temperatures closer to the surrounding soil, experience less seasonal temperature variability, resulting in a more reliable system for storing heat through colder seasons.
- The electricity generated by the PV modules is largely consumed within the system due to the high power demands of its components, resulting in near-zero net power surplus and minimal grid injection for both the centralised and decentralised case.
- Considering maximum temperatures of 25 ° C and 30 ° C, the optimal solutions for the case study lie at a 95 m radius for 25 ° C and a 75 m radius for 30 ° C, corresponding to volumes of around 315 000 m^3 and 175 000 m^3, respectively. A relatively larger aquifer offers advantages to ensure system reliability, reducing the risk of exceeding the maximum temperature and enhancing system stability by making it less dependent on seasonal changes.

In addition, we have the following recommendations for future research based on this work:

- Despite our conclusions suggesting that the losses in the piping are neglectable with respect to the losses in the ATES, finding optimal routing paths for the thermal network would be beneficial in terms of highly efficient distribution systems.
- Elaborate on the modelling of the buildings' heating network to provide a more accurate representation of the thermal demand. Possible improvements include: considering the effects of the occupants, appliances, the ventilation system of the building, and heating through the windows due to irradiance.
- Since most heat pumps and district heating networks allow it, including cooling demand could provide insight into the additional value of district heating networks for cooling applications.

CRediT authorship contribution statement

Ties Beijneveld: Writing – review & editing, Writing – original draft, Methodology, Investigation, Formal analysis, Conceptualization. **Joel Alpízar-Castillo:** Writing – original draft, Validation, Supervision, Methodology, Formal analysis. **Laura Ramírez-Elizondo:** Writing – review & editing, Validation, Supervision.

Declaration of competing interest

The authors declare the following financial interests/personal relationships which may be considered as potential competing interests: Laura Ramirez-Elizondo reports financial support was provided by Netherlands Enterprise Agency. If there are other authors, they declare that they have no known competing financial interests or personal relationships that could have appeared to influence the work reported in this paper.

Data availability

No data was used for the research described in the article.

References

[1] International Energy Agency, Statistics report Key World Energy Statistics 2021, Technical Report, 2021.
[2] International Energy Agency, The Netherlands Energy Mix, 2023, URL https://www.iea.org/countries/the-netherlands/energy-mix.
[3] J. Pool, E. Schouten, O. Van Rieven, T. Bal, R. Spuijbroek, Rapport Vooronderzoek Duurzaam Werfgebied Naar een energiepositieve Werf: Het kan als je het wil!, Technical Report, HET, 2023, URL https://hetcooperatie.nl/category/uncategorized/.
[4] T. Beijneveld, Photovoltaic Thermal System Design Including Aquifer Thermal Energy Storage in a Fifth Generation District Heating Network in Hilversum (Master's thesis), Delft University of Technology, 2024, URL https://repository.tudelft.nl/record/uuid:5b7db8b5-fbca-4eb5-89f1-ddf53f7487a8.
[5] N. Damianakis, G.R.C. Mouli, P. Bauer, Grid impact of photovoltaics, electric vehicles and heat pumps on distribution grids — An overview, Appl. Energy 380 (2025) 125000, http://dx.doi.org/10.1016/j.apenergy.2024.125000, URL https://www.sciencedirect.com/science/article/pii/S0306261924023845.
[6] J. Alpízar-Castillo, L. Ramírez-Elizondo, P. Bauer, The effect of non-coordinated heating electrification alternatives on a low-voltage distribution network with high PV penetration, in: 2023 IEEE 17th International Conference on Compatibility, Power Electronics and Power Engineering (CPE-POWERENG), 2023, pp. 1–6, http://dx.doi.org/10.1109/CPE-POWERENG58103.2023.10227394.
[7] G. Li, M. Li, R. Taylor, Y. Hao, G. Besagni, C. Markides, Solar energy utilisation: Current status and roll-out potential, Appl. Therm. Eng. 209 (2022) 118285, http://dx.doi.org/10.1016/j.applthermaleng.2022.118285.
[8] I. Sarbu, C. Sebarchievici, A comprehensive review of thermal energy storage, Sustainability 10 (1) (2018) http://dx.doi.org/10.3390/su10010191, URL https://www.mdpi.com/2071-1050/10/1/191.
[9] P. Mokhberi, P. Mokhberi, M. Izadi, M. Bagheri Nesaii, W. Yaici, F. Minelli, Thermal regulation enhancement in multi-story office buildings: Integrating phase change materials into inter-floor void formers, Case Stud. Therm. Eng. 60 (2024) 104792, http://dx.doi.org/10.1016/j.csite.2024.104792.
[10] Men in green B.V., The flower farm, Care to change, Werkplaats hanegraaf, Build this up, Imediate holding B.V., Elcheapo B.V., ENERGIE POTENTIEELSCAN, Technical Report, TNO, 2017.
[11] E. Khlebnikova, I. Pothof, S. van der Zwan, L. Loverdou, On the design of 5GDHC substation control systems, Int. J. Sustain. Energy 43 (1) (2024) 1–16, http://dx.doi.org/10.1080/14786451.2024.2317141.
[12] S. Jansen, S. Mohammadi, R. Bokel, Developing a locally balanced energy system for an existing neighbourhood, using the 'smart urban isle' approach, Sustain. Cities Soc. 64 (2021) 102496, http://dx.doi.org/10.1016/J.SCS.2020.102496.
[13] S. Picone, M. Bloemendal, M. Pellegrini, N. Hoekstra, A. Andreu Gallego, J. Rodriguez Comins, A. Murrel, Novel combinations of aquifer thermal energy storage with solar collectors, soil remediation and other types of geothermal energy systems, in: European Geothermal Congress 2019 Den Haag, 2019, pp. 11–14, URL https://resolver.tudelft.nl/uuid:78512f51-b202-4f86-a2ee-a8bfa42618cf.
[14] J. Jebamalai, K. Marlein, J. Laverge, Influence of centralized and distributed thermal energy storage on district heating network design, Energy 202 (2020) 117689, http://dx.doi.org/10.1016/J.ENERGY.2020.117689.
[15] J. Röder, B. Meyer, U. Krien, J. Zimmermann, T. Stührmann, E. Zondervan, Optimal design of district heating networks with distributed thermal energy storages – method and case study, Int. J. Sustain. Energy Plan. Manag. 31 (2021) 5–22, http://dx.doi.org/10.5278/IJSEPM.6248.
[16] T. Nuytten, B. Claessens, K. Paredis, J. Van Bael, D. Six, Flexibility of a combined heat and power system with thermal energy storage for district heating, Appl. Energy 104 (2013) 583–591, http://dx.doi.org/10.1016/J.APENERGY.2012.11.029.
[17] M. Geraedts, J. Alpizar-Castillo, L. Ramirez-Elizondo, P. Bauer, Optimal sizing of a community level thermal energy storage system, MELECON 2022 - IEEE Mediterr. Electrotech. Conf. Proc. (2022) 52–57, http://dx.doi.org/10.1109/MELECON53508.2022.9842945, URL https://repository.tudelft.nl/islandora/object/uuid%3A0fb9de75-2308-4732-b12e-daf816f044ea.
[18] G.S. Krishna Priya, M.S. Thakare, P.C. Ghosh, S. Bandyopadhyay, Sizing of standalone photovoltaic thermal (PVT) systems using design space approach, Sol. Energy 97 (2013) 48–57, http://dx.doi.org/10.1016/J.SOLENER.2013.08.003.
[19] D. Testi, E. Schito, P. Conti, Cost-optimal sizing of solar thermal and photovoltaic systems for the heating and cooling needs of a nearly zero-energy building: Design methodology and model description, Energy Procedia 91 (2016) 517–527, http://dx.doi.org/10.1016/J.EGYPRO.2016.06.191.
[20] M. Barbu, M. Siroux, G. Darie, Numerical model and parametric analysis of a liquid based hybrid photovoltaic thermal (PVT) collector, Energy Rep. 7 (2021) 7977–7988, http://dx.doi.org/10.1016/J.EGYR.2021.07.058.
[21] J. Alpízar-Castillo, L.M. Ramírez-Elizondo, P. Bauer, Modelling and evaluating different multi-carrier energy system configurations for a dutch house, Appl. Energy 364 (2024) 123197, http://dx.doi.org/10.1016/J.APENERGY.2024.123197.
[22] R.Y. Wong, C.Y. Tso, S.Y. Jeong, S.C. Fu, C.Y. Chao, Critical sky temperatures for passive radiative cooling, Renew. Energy 211 (2023) 214–226, http://dx.doi.org/10.1016/J.RENENE.2023.04.142.
[23] K.S. Lee, A review on concepts, applications, and models of aquifer thermal energy storage systems, Energies 3 (6) (2010) 1320–1334, http://dx.doi.org/10.3390/en3061320.
[24] R.K. Singh, R.V. Sharma, Numerical analysis for ground temperature variation, Geotherm. Energy 5 (1) (2017) 1–10, http://dx.doi.org/10.1186/S40517-017-0082-Z/FIGURES/11, URL https://geothermal-energy-journal.springeropen.com/articles/10.1186/s40517-017-0082-z.
[25] M. Bloemendal, N. Hartog, Analysis of the impact of storage conditions on the thermal recovery efficiency of low-temperature ATES systems, Geothermics 71 (2018) 306–319, http://dx.doi.org/10.1016/J.GEOTHERMICS.2017.10.009.

[26] W. Van Dalfsen, The shallow subsurface temperature field in the netherlands, Adv. Eur. Geotherm. Res. (1980) 496–505, http://dx.doi.org/10.1007/978-94-009-9059-3{_}44, URL https://link.springer.com/chapter/10.1007/978-94-009-9059-3_44.
[27] M. Boers, H. van Hateren, Gebiedsstudie bodemenergie, Technical Report, VHGM B.V., Hilversum, 2024.
[28] D. Wessel, ASHRAE Handbook-fundamentals, 'Comstock, Stephen', 2001.
[29] N. Damianakis, G.C.R. Mouli, P. Bauer, Risk-averse estimation of electric heat pump power consumption, in: CPE- POWERENG 2023 - 17th IEEE International Conference on Compatibility, Power Electronics and Power Engineering, Institute of Electrical and Electronics Engineers (IEEE), 2023, http://dx.doi.org/10.1109/CPE-POWERENG58103.2023.10227424, URL https://research.tudelft.nl/en/publications/risk-averse-estimation-of-electric-heat-pump-power-consumption.
[30] Productblad Qpanel (HEN), 2024, URL https://www.hr-energy.com/media/bjqpqxuc/productblad-qpanel-pvt-paneel-1722.pdf.
[31] Z. Sun, Q. Cui, Q. Wang, J. Ning, J. Guo, B. Dai, Y. Liu, Y. Xu, Experimental study on CO2/R32 blends in a water-to-water heat pump system, Appl. Therm. Eng. 162 (2019) 114303, http://dx.doi.org/10.1016/J.APPLTHERMALENG.2019.114303.
[32] S. Bordignon, J.D. Spitler, A. Zarrella, Simplified water-source heat pump models for predicting heat extraction and rejection, Renew. Energy 220 (2024) 119701, http://dx.doi.org/10.1016/J.RENENE.2023.119701.
[33] E. Blokker, Q. Pan, Invloed warmtenetten op temperatuur drinkwater. Resultaten TKI Engine, Technical Report, TKI Engine, 2022, URL https://library.kwrwater.nl/publication/69401440/invloed-warmtenetten-op-temperatuur-drinkwater-resultatentki-engine/.
[34] P. Wallentén, Steady-state heat loss from insulated pipes, 1991, URL https://portal.research.lu.se/en/publications/steady-state-heat-loss-from-insulated-pipes.
[35] Nowtricity, Nowtricity, 2024.
[36] A. Virtuani, A. Borja Block, N. Wyrsch, C. Ballif, The carbon intensity of integrated photovoltaics, Joule 7 (11) (2023) 2511–2536, http://dx.doi.org/10.1016/J.JOULE.2023.09.010.
[37] J. Godinaud, P. Loubet, S. Gombert-Courvoisier, A. Pryet, A. Dupuy, F. Larroque, Life cycle assessment of an aquifer thermal energy storage system: Influence of design parameters and comparison with conventional systems, Geothermics 120 (2024) http://dx.doi.org/10.1016/J.GEOTHERMICS.2024.102996.
[38] N. Hoekstra, J. Valstar, Aquifer thermal energy storage, Technical Report, Deltares, 2024, URL https://www.deltares.nl/en/expertise/areas-of-expertise/energy-transition/aquifer-thermal-energy-storage.